Chaotic fluctuations in a universal set of transmon qubit gates

Daniel Basilewitsch,[1] Simon-Dominik Börner,[2] Christoph Berke,[2]
Alexander Altland,[2] Simon Trebst,[2] and Christiane P. Koch[1,*]

[1]*Dahlem Center for Complex Quantum Systems and Fachbereich Physik, Freie Universität Berlin, D-14195 Berlin, Germany*
[2]*Institute for Theoretical Physics, University of Cologne, D-50937 Cologne, Germany*

(Dated: November 27, 2023)

Transmon qubits arise from the quantization of nonlinear resonators, systems that are prone to the buildup of strong, possibly even chaotic, fluctuations. One may wonder to what extent fast gate operations, which involve the transient population of states outside the computational subspace, can be affected by such instabilities. We here consider the eigenphases and -states of the time evolution operators describing a universal gate set, and analyze them by methodology otherwise applied in the context of many-body physics. Specifically, we discuss their spectral statistic, the distribution of time dependent level curvatures, and state occupations in- and outside the computational subspace. We observe that fast entangling gates, operating at speeds close to the so-called quantum speed limit, contain transient regimes where the dynamics indeed becomes partially chaotic. We find that for these gates even small variations of Hamiltonian or control parameters lead to large gate errors and speculate on the consequences for the practical implementation of quantum control.

I. INTRODUCTION

Coupled superconducting circuits are one of the leading platforms in quantum information science [1, 2]. In this architecture, the nonlinearity of Josephson junctions serves to separate an energetically low-lying qubit subspace from a higher-lying state space whose presence is often ignored. The restriction to the computational subspace rests on the assumption that the energy stored in the initial state remains decentralized, and higher excited states of individual 'qubits' are not accessed. This condition is, however, not necessarily satisfied. For example, the tunneling bridges in arrays of superconducting qubits imply the presence of residual qubit-qubit couplings which can be made algebraically, but never exponentially, small in the detuning from the resonator frequencies. Depending on the choice of couplings and detunings inherent to a given qubit architecture, this may compromise the stationarity of spatially 'delocalized' states and lead to strong fluctuations in the qubit register due to energetically high-lying single-particle excitations [3].

When operating superconducting circuits beyond merely storing information, population of energy levels outside of the computational subspace is rather common. It occurs whenever fast manipulation of qubits is required, be it for gate operation [4] or qubit reset [5]. Fast device operation is desirable in view of optimal clock speeds but also to combat decoherence. The shortest possible time in which a given task can be carried out is referred to as the quantum speed limit (QSL) [6]. When implementing quantum gates, the QSL is fundamentally determined by the size of the effective time-dependent qubit-qubit couplings. This is because the couplings are needed to generate entanglement — or, in the case of local rotation gates, undo undesired entanglement that is due to the residual couplings. Then, population of higher lying levels during the gate operation can easily be brought back to the computational subspace at the end of the gate by suitably tailored pulses [7]. On this basis, one may assume that the anharmonicity defining the energetic separation of the computational subspace from the higher lying state space does not limit the operation time for quantum gates.

In this paper we point out the existence of an independent second mechanism potentially impeding the stability of gates at fast operation times: from the perspective of (classical) nonlinear dynamics, the time evolution of coupled transmons takes place in a twilight zone between integrable dynamics realized in the limit of weak inter-transmon coupling and strong, possibly even chaotic fluctuations at larger couplings [8, 9]. Quantum mechanically, this ambiguity shows in the structure of transmon array many-body spectra which generically show statistical signatures of both integrability (evidenced by Poisson statistics) and chaos (Wigner-Dyson statistics) [3]. From the same perspective, a transmon gate is a driven protocol transiently exciting a subsystem of qubits close to the ones targeted by the gate operation. The faster a gate operation, the higher the chances that it connects to semiclassically unstable sectors of the state space [8].

The full information on a gate operation is encoded in the instantaneous eigenvalues and –states of the unitary operator $\mathrm{U}(t)$ implementing it. This operator is subject to external time dependence, imposed via optimal control [10] to realize an intended map in the computational state, but transiently acting in the larger space of high-lying states. In this paper, we will apply methodology borrowed from quantum nonlinear dynamics and many-body localization theory to explore its properties, and hint at potential stability issues. To be specific, we consider a universal gate set on the smallest possible structure comprising two transmon qubits coupled via an intermediate cavity [7], see Fig. 1(a). We will analyze statistical properties of the instantaneous eigenspectra of the corresponding operators, and compare to the extreme limiting distributions integrable/Poisson vs. chaotic/Wigner-Dyson. We will also analyze the distribution of the *curvatures* of the time-dependent levels as a signature whose relevance in the context of many-body localization theory has been the subject of recent research [11]. At the same time, they are of applied relevance since the curvature of nearby levels determines the

* christiane.koch@fu-berlin.de

state distribution in a driven protocol. We will discuss the transient distribution of spectral weight during the protocol in states outside the computational subspace. Since the non-computational space will be harder to control under conditions affected by traces of chaotic dynamics and/or uncertainties due to device imperfections, its occupation on operation must be a factor entering the overall stability of the gate. To assess the cumulative effect of these structures, we will, finally, consider gate errors caused by variations in the model Hamiltonian or the parameters used for the control protocol.

A key result of our analysis will be that traces of nonlinear and even chaotic dynamics are visible in the operators implementing fast gates. At the same time, they present no principal obstruction to high gate fidelities. The reason is the finite dimensionality of the effective Hilbert space subject to control. While classical chaotic time evolution is unpredictable by definition, projection onto a finite dimensional quantum Hilbert space leads to a more tame dynamics, which can be optimized towards a desired output. Crucially, however, nonlinearity correlates with a high sensitivity of gate fidelities to just very small modifications in the Hamiltonian parameters. A systematic study of these effects and their applied impact on the quantum control of fast gate operations will be the subject of followup research.

The rest of the paper is organized as follows. We briefly review the model and gate operations of Ref. [7] in Sec. II and discuss our results in Sec. III. This includes the spectral analysis via the eigenphases of the time evolutions implementing the gates in Sec. III A and the eigenphase curvature distributions in Sec. III B. We examine the populations of eigenstates in Sec. III C, followed by a robustness analysis in Sec. III D and conclude in Sec. IV. For completeness, we present the (less conclusive) analysis of out-of-time-ordered correlators (OTOCs) in Appendix A.

II. MODEL AND CONTROL PROTOCOLS

We will analyze two universal sets of gates, with Hadamard and local phase gates as representative single-qubit operations and the BGATE as entangling operation. The choice of the latter was motivated by the fact that it yields the smallest decomposition of an arbitrary two-qubit operation into gates of a universal set [12]. (For full operability of the quantum hardware, it is important to inspect a complete universal set, as this requires the ability to both create and destroy entanglement.) The gates we analyze have been derived using optimal control theory for two transmon qubits with a joint transmission line cavity subject to a microwave drive [7]. In a frame rotating with the drive frequency ω_d, the Hamiltonian reads

$$\begin{aligned}\mathsf{H}(t) \;=\; &\sum_{q=1}^{2}\left[\delta_q \mathsf{b}_q^\dagger \mathsf{b}_q + \frac{\alpha_q}{2}\mathsf{b}_q^\dagger \mathsf{b}_q^\dagger \mathsf{b}_q \mathsf{b}_q + g\left(\mathsf{b}_q^\dagger \mathsf{a} + \mathsf{b}_q \mathsf{a}^\dagger\right)\right] \\ &+\delta_\mathrm{c}\mathsf{a}^\dagger\mathsf{a} + \frac{1}{2}\mathcal{E}(t)\mathsf{a} + \frac{1}{2}\mathcal{E}^*(t)\mathsf{a}^\dagger\,, \end{aligned} \tag{1}$$

where b_q and a are the annihilation operators for the qth transmon and the cavity, respectively, $\delta_q = \omega_q - \omega_\mathrm{d}$ and $\delta_\mathrm{c} = \omega_\mathrm{c} - \omega_\mathrm{d}$ the qubit and cavity detunings from the drive frequency ω_d, respectively, α_q the qubit anharmonicities, and g is the qubit-cavity coupling strength. $\mathcal{E}(t)$ denotes the time-dependent amplitude of the cavity drive; it is the control knob that is tuned to implement the desired qubit dynamics. Table I provides an overview of all relevant parameters.

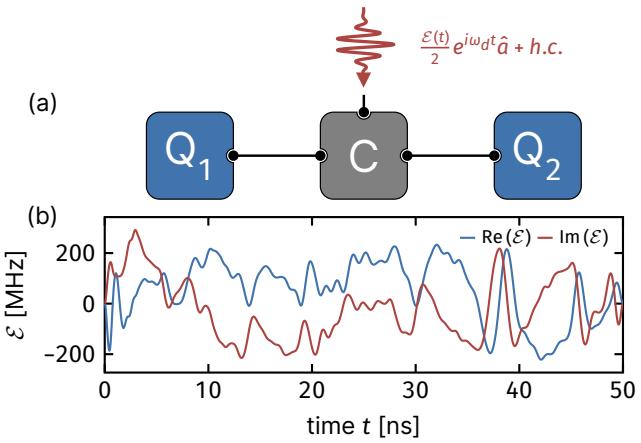

FIG. 1. **Schematic overview of the transmon-cavity system** consisting of (a) two transmon qubits Q_1,Q_2 coupled via a joint transmission line cavity C. Gates are implemented by applying a fine-tuned microwave drive with envelope $\mathcal{E}$ to the common cavity. (b) Example of a fine-tuned drive tone, implementing an entangling BGATE with a gate duration of 50 ns.

TABLE I. Parameters for the system illustrated in Fig. 1(a) consisting of two transmons, Q_1 and Q_2, and a cavity C. Taken from Ref. [7].

frequency cavity C	$\omega_\mathrm{c}/2\pi$	6.2 GHz
base frequency transmon Q_1	$\omega_1/2\pi$	6.0 GHz
base frequency transmon Q_2	$\omega_2/2\pi$	5.9 GHz
anharmonicity transmon Q_1	$\alpha_1/2\pi$	−290 MHz
anharmonicity transmon Q_2	$\alpha_2/2\pi$	−310 MHz
coupling between transmons and cavity	$g/2\pi$	70 MHz
driving frequency of cavity C	$\omega_\mathrm{d}/2\pi$	5.93 GHz

The quantum gates that we will analyze, operate in the quasi-dispersive straddling qutrits (QuaDiSQ) regime where multiple sources of entanglement interfere simultaneously. As a result, the cavity cannot be adiabatically eliminated and transmon levels outside the computational subspace are exploited for fast gate operation [7]. The Hilbert space is thus the tensor product of the Hilbert spaces of the two transmons and the cavity. Numerically, taking the local Hilbert space dimensions to be 5 for each of the transmons and 6 for the cavity, resulting in a total Hilbert space dimension of 150, turned out to be sufficient for convergence. Note that in the QuaDiSQ regime, the computational states $|00\rangle, |01\rangle, |10\rangle, |11\rangle$ are the *dressed* basis states as they are eigenstates of the system in the absence of the control field and thus do not change further once the gate protocol is finished. In detail, $|i_1 i_2\rangle$ refers to the eigenstate of H, cf. Eq. (1), with $\mathcal{E}(t) = 0$, which has the largest overlap with the bare Fock state $|i_1\rangle\otimes|i_2\rangle\otimes|i_\mathrm{c}=0\rangle = |i_1, i_2, 0\rangle_\mathrm{Fock}$, where i_1, i_2 and i_c label the excitations of the

two transmons and the cavity.

The fasted possible universal set of gates uses gate durations of $T = 50\,\mathrm{ns}$ [7]. This limit is set by the local gates, whereas the fastest entangling operation, $\sqrt{i\mathsf{SWAP}}$, requires only about $10\,\mathrm{ns}$ [7]. The fast gate operations come at the expense of complex and spectrally broad pulse shapes $\mathcal{E}(t)$, see Fig. 1(b) for an example. Increasing the gate durations by a factor of two to $T = 100\,\mathrm{ns}$ significantly reduces both temporal and spectral complexity of the pulses [7].

III. RESULTS

Signatures of quantum chaos in transmon arrays have recently been identified via an analysis of their spectral statistics and deviations of their eigenstates from the localized states of fully decoupled qubits [3, 8]. In the following, we investigate whether the principles underlying these observations also show in the dynamics of gate operations. To this end, the tools applied in [3, 8] first need to be adapted to the analysis of externally imposed time evolution.

A. Kullback-Leibler divergence

A quantitative analysis of many-body spectra including their cross-over from Wigner-Dyson to Poissonian statistics, i.e., from strongly correlated chaotic states to uncorrelated localized states is furnished by the Kullback-Leibler (KL) divergence [3]. The simplest extension to analyze the gate dynamics would be to calculate the KL divergence for the instantaneous eigenvalues of the Hamiltonian $\mathsf{H}(t)$, cf. Eq. (1). However, this captures only time-local information. In contrast, the time evolution operator $\mathsf{U}(t) \in \mathrm{SU}(N)$, with N the Hilbert space dimension, contains information about the entire dynamics up to time t. We therefore analyze the eigenphases of $\mathsf{U}(t)$ rather than the eigenvalues of $\mathsf{H}(t)$.

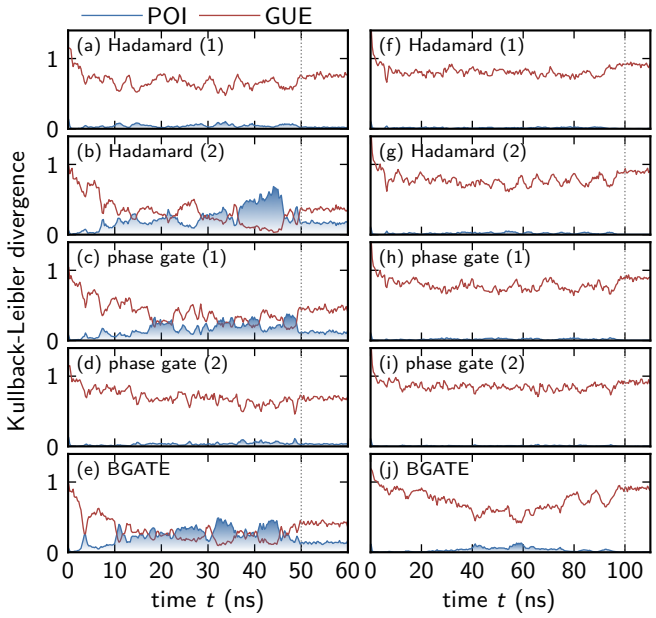

FIG. 2. **Spectral analysis of chaotic fluctuations in single-qubit and two-qubit gates** of two transmon qubits in the QuaDiSQ regime [7]: The statistics of the relative eigenphase differences of the time evolution, $\{R_n(t)\}$, cf. Eq. (2), are compared to Poisson (POI), resp. Gaussian (GUE) statistics using the Kullback-Leibler (KL) divergence (4) for gate durations of $T = 50\,\mathrm{ns}$ (left) and $T = 100\,\mathrm{ns}$ (right). Deviations from Poisson statistics, observed clearly in panels (b), (c) and (e) and to a lesser extent in panels (a), (d) and (j), indicate emergent quantum chaotic fluctuations.

The instantaneous eigenvalues of $\mathsf{U}(t)$, $\lambda_1(t), \ldots, \lambda_N(t) \in \mathbb{C}$, are all of magnitude one and thus have a unique representation, $\lambda_n(t) = e^{\mathrm{i}\phi_n(t)}$, $n = 1, \ldots, N$, in terms of their eigenphases, $\phi_1(t), \ldots, \phi_N(t) \in [-\pi, \pi)$. Without loss of generality, we assume $\phi_1(t) \leq \phi_2(t) \leq \cdots \leq \phi_N(t)$ for every time t [13] and define nearest neighbor differences as $\Delta\phi_n(t) \equiv \phi_{n+1}(t) - \phi_n(t)$, $n = 1, \ldots, N-1$. The corresponding relative differences are then given as [14]

$$r_n(t) = \frac{\Delta\phi_n(t)}{\Delta\phi_{n+1}(t)}\,, \quad R_n(t) = \min\left\{r_n(t), \frac{1}{r_n(t)}\right\} \tag{2}$$

with $n = 1, \ldots, N-2$. The definition of the $R_n(t)$, in contrast to that of the $r_n(t)$, ensures values within the interval $[0, 1]$ which is convenient for statistical analysis.

In the limiting cases of integrable, resp. chaotic dynamics, the relative eigenphase differences $\{R_n(t)\}$ are expected to obey Poissonian, respectively Wigner-Dyson statistics. Up to inessential corrections [15] [16], the corresponding distributions are given by

$$P_{\mathrm{POI}}(R) = \frac{2}{(1+R)^2}\,, \tag{3a}$$

$$P_{\mathrm{GUE}}(R) = \frac{162\sqrt{3}}{4\pi}\frac{(R+R^2)^2}{(1+R+R^2)^4}, \tag{3b}$$

Only in limiting cases will the observed distribution $P_{\mathrm{rel.}}$ of $\{R_n(t)\}$ be described by Eq. (3). Deviations from the limiting cases P_{POI} or P_{GUE} can be quantified using the Kullback-Leibler (KL) divergence, in analogy to the spectral analysis of the static qubit arrays [3]. The KL divergence as a distance measure between two statistical distributions P_1 and P_2 , defined over some probability space $\mathcal{R}$, is given by [17]

$$D_{\mathrm{KL}}(P_1|P_2) = \sum_{R\in\mathcal{R}} P_1(R)\log\left(\frac{P_1(R)}{P_2(R)}\right)\,, \tag{4}$$

where P_1 and P_2 are normalized such that $\sum_{R\in\mathcal{R}} P_1(R) = \sum_{R\in\mathcal{R}} P_2(R) = 1$. In general $D_{\mathrm{KL}}(P_1|P_2) \neq D_{\mathrm{KL}}(P_2|P_1)$. We therefore normalize the KL divergences individually such that $D_{\mathrm{KL}}(P_{\mathrm{GUE}}|P_{\mathrm{POI}}) = 1$ and $D_{\mathrm{KL}}(P_{\mathrm{POI}}|P_{\mathrm{GUE}}) = 1$. Since we expect the actual distribution $P_{\mathrm{rel.}}$ to be a mixture of P_{POI} and P_{GUE}, this normalization is a convenient way to ensure $0 \leq D_{\mathrm{KL}}(P_{\mathrm{rel.}}|P_{\mathrm{POI}}), D_{\mathrm{KL}}(P_{\mathrm{rel.}}|P_{\mathrm{GUE}}) \leq 1$. When comparing the probability distribution $P_{\mathrm{rel.}}$ of the relative eigenphase differences $\{R_n(t)\}$ to Poisson (POI) statistics, a non-zero KL divergence signals the emergence of statistical correlations. Conversely, chaotic fluctuations show in the KL divergence to P_{GUE} approaching zero.

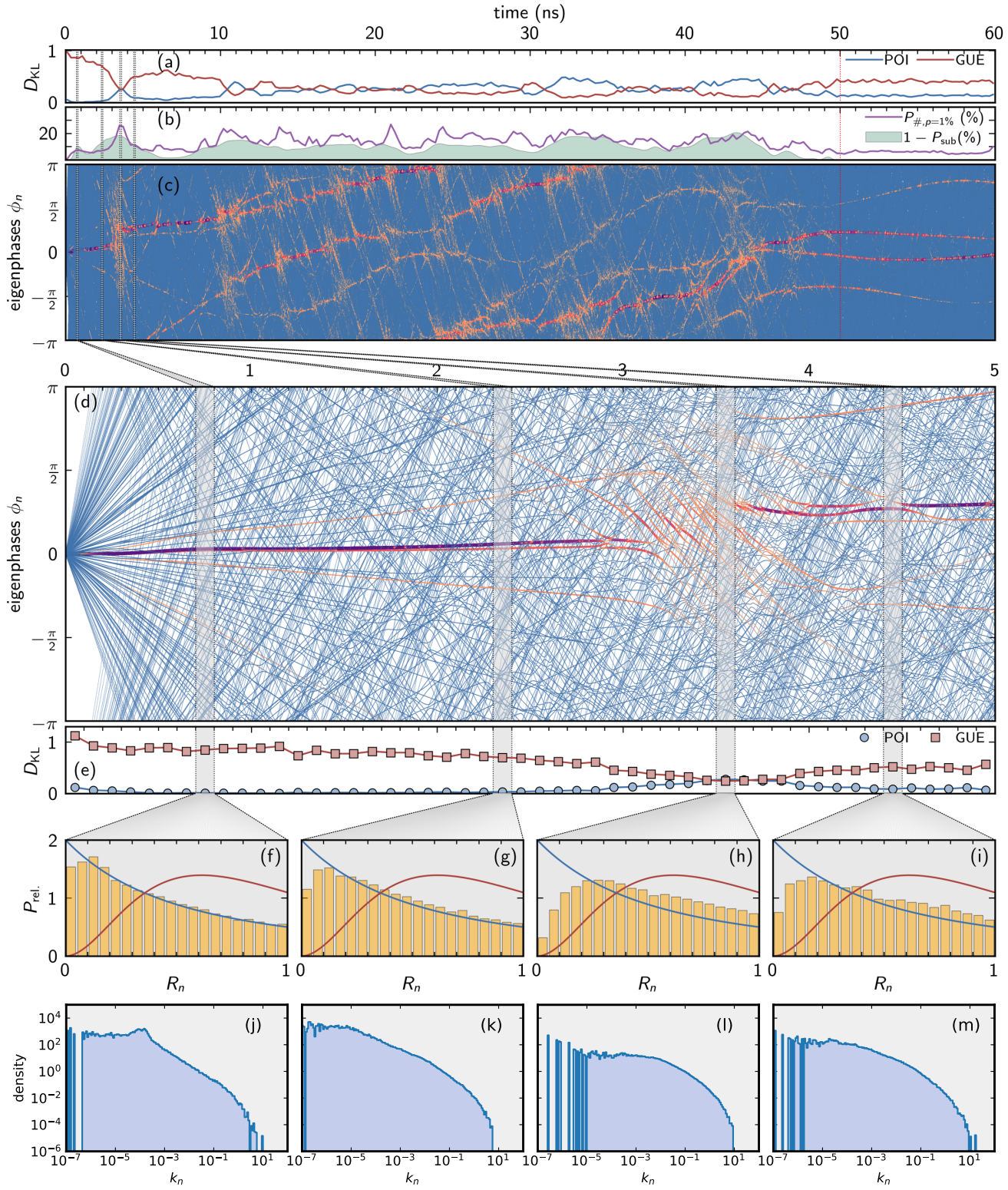

FIG. 3. **Detailed spectral analysis of the entangling BGATE** with $T = 50\,\text{ns}$. (a), (e): Kullback-Leibler divergences as in Fig. 2(e) with the red dotted line indicating the gate time T. The data for $t > T$ are obtained by time evolution with $\mathcal{E}(t) = 0$. (b): Population outside the computational subspace (green area) and percentage of $\mathsf{U}(t)$-eigenstates $\{|\Phi_n(t)\rangle\}$ with population $p_n(t) \geq 1\%$ for the initial state $|00\rangle$, cf. Eq. (9). (c), (d): Instantaneous eigenphases $\{\phi_n(t)\}$ of $\mathsf{U}(t)$ (blue lines) with their population $p_i(t)$ indicated by size and color of the dots. (f)–(i): Probability distributions of the relative eigenphases $\{R_n(t)\}$, cf. Eq. (2), in the time intervals highlighted in gray in panels (a)–(e). The ideal Poisson and Gaussian distributions are shown by blue and red lines. (j)–(m): Dimensionless level curvatures $k_n(t)$ for the intervals analyzed in (f)–(i).

Figure 2 shows the KL divergence for the probability distribution of the $\{R_n(t)\}$ when compared to ideal Poisson (POI) or Wigner-Dyson (GUE) statistics. To evaluate Eq. (4), we extract P_1 from the numerical data, whereas P_2 follows one of the ideal distributions. To gather enough statistical data, we divide the entire time span into 250 intervals and collect all R_n values from a fixed interval, yielding a single, joint distribution $P_{\text{rel.}}^{\text{joint}}$ for each interval. For these joint distributions, we then calculate the Kullback-Leibler divergences and display them in Fig. 2 at the respective interval midpoint. While the KL divergence with respect to the Poisson distribution $D_{\text{KL}}(P_{\text{rel.}}|P_{\text{POI}})$ vanishes almost everywhere for the slower set of gates (right column of Fig. 2), the gates at the quantum speed limit in the left column of Fig. 2 show chaotic fluctuations. When inspecting the different gates, the Hadamard gate on the first qubit and the local phase gate on the second qubit seem much less prone to signatures of chaos. This can be attributed to the much weaker driving that is used to implement these gates with peak amplitudes of at most 200 MHz compared to 300 MHz for the other three gates in the left column of Fig. 2 [7]. Note that these amplitudes are of a similar order of magnitude as the anharmonicities, cf. Table I.

We examine one of the fast gates with chaotic fluctuations in the dynamics, the BGATE, more closely in Fig. 3. Panel (c) shows the eigenphases $\phi_n(t)$ of the time-evolution operator $\mathsf{U}(t)$ for the corresponding dynamics as blue lines. Due to their high density, they appear as a blue area. Figure 3(d) therefore provides a blow-up of the first 5 ns of the dynamics. This time frame is particularly interesting because it shows the transition from straight lines and line crossings for all $\phi_n(t)$ into a regime where avoided crossings between lines start to become more frequent. This transition starts roughly at $t \approx 1\,\text{ns}$. Moreover, the dynamics within the first 5 ns also shows chaotic behavior, namely in the time frame between 3 ns and 4 ns. The emerging many-body nonlinear behavior is witnessed by the KL divergence of the eigenphases $\phi_n(t)$, cf. Eq. (2), as shown in Fig. 3(a) for the total protocol and a blow-up of the first 5 ns in Fig. 3(e). While up to $t \approx 3\,\text{ns}$, the KL divergence shows an almost perfect match with an ideal POI statistics, evidencing non-chaotic behavior, it diverges from POI statistics and shows a larger match with GUE statistics, signalling chaotic behavior, between 3 ns and 4 ns. Figure 3(f)–(i) shows the actual distribution $P_{\text{rel.}}$ at four representative times. In panel (f), avoided crossings do not yet play a role and an almost perfect match of $P_{\text{rel.}}$ with ideal POI statistics, shown as blue line, is observed. Figure 3(g) and (i) are evaluated at times before and after the chaotic regime between 3 ns and 4 ns, respectively. In both cases, similarities of $P_{\text{rel.}}$ to POI statistics dominate. In contrast, the statistics in Fig. 3(h) is evaluated within the chaotic $3-4$ ns time frame and shows a stronger match with GUE statistics, displayed in red in panels (f)–(i).

It is interesting to see in Fig. 3 that after 4 ns the dynamics becomes less chaotic again. Such emergence and disappearance of chaos occurs several times over the entire protocol duration and can also be observed for the other fast gates in Fig. 2, for which the KL divergences indicate chaotic behavior. Remarkably, the (re)emergence of chaotic behavior does not have any negative impact on the gate errors, as the latter are identically small for both the fast and slow protocols in Fig. 2. The optimized control field seems to navigate the computational basis states safely through the chaotic regions.

There are two points to note about the calculations presented in Fig. 3. First, similar to Fig. 2, we calculate the KL divergence within time slices $[\tau_i, \tau_{i+1})$ which are of length 0.1 ns in Fig. 3(a) and (e). Second, we calculate it using all eigenphases $\phi_n(t)$, i.e., all blue lines, and not just the fraction of eigenphases $\phi_n(t)$ for which the corresponding eigenstate $|\Phi_n(t)\rangle$ of $\mathsf{U}(t)$ shows a significant overlap with the time-evolved computational states $|00\rangle, |01\rangle, |10\rangle, |11\rangle$. We will discuss the latter in more detail in Sec. III C but note at this stage, that the color code in Fig. 3(c) and (d) shows how the computational basis states 'evolve' from initial to final time exemplarily for $|00\rangle$. Larger and darker (smaller and brighter) dots indicate that the time-evolved state $|\Psi_{00}(t)\rangle = \mathsf{U}(t)\,|00\rangle$ has a larger (smaller) overlap with the eigenstate $|\Phi_n(t)\rangle$ to which the blue line corresponds. A condensed version of this is shown as purple line in Fig. 3(b), presenting the fraction of eigenstates $\{|\Phi_n(t)\rangle\}$ that have at least an absolute-squared overlap of 1% with the time-evolved state $|\Psi_{00}(t)\rangle$. This is an indicator of how local/non-local the time-evolved state $|\Psi_{00}(t)\rangle$ becomes when expanded via the instantaneous eigenstates $\{|\Phi_n(t)\rangle\}$. In addition, the green area in Fig. 3(b) indicates the fraction of population that is outside of the computational subspace.

In the following, we seek further measures that allow to discriminate between chaotic and non-chaotic regimes in the dynamics but are – ideally – more directly linked to the gate performance. This is a limitation of the KL divergences inspected so far which have been evaluated for the statistics of all the eigenstates $\{|\Phi_n(t)\rangle\}$, respectively eigenphases $\phi_n(t)$, of the time-evolution operator $\mathsf{U}(t)$. While it is able to discriminate between chaotic and non-chaotic regimes in the overall time-evolution, it is a state-independent metric and thus does not contain any information about the dynamics of the actual computational states $|00\rangle, |01\rangle, |10\rangle, |11\rangle$ for which the control field, and thus $\mathsf{U}(t)$, have been optimized. To this end, a common approach is to use out-of-time-ordered correlators (OTOCs) [18]. However, we do not find OTOCs to be reliable indicators of chaotic regimes, cf. Appendix A, in line with findings for bosons in a double well [19]. In contrast, a measure that is sensitive to the evolution of the computational basis states and can be a good indicator of chaos, is to analyze the population dynamics as we do in Sec. III C. Before that, we briefly discuss the curvature distributions of the eigenphases (sharing the weakness of state-insensitivity with the KL divergence) as an indicator of non-linear dynamics in the next section.

B. Curvature distributions

Beyond the statistics of eigenphases, the structure of avoided crossings can be another indicator of nonlinear dynamics. Consider the evolution of two nearby phases $\phi_n(t)$ and $\phi_m(t)$. If they are statistically uncorrelated, they may

cross, and a glance at Fig. 3 shows that this is the generic situation in the early stages of the time evolution. Correlations, on the other hand, lead to effective phase repulsion, and to an overall more 'curvy' pattern of phase evolutions. To quantify this structure, we consider the curvature κ_n of the eigenphases,

$$\kappa_n(t) = \frac{d^2\phi_n(t)}{dt^2}\,. \tag{5}$$

As with the level spacings, the curvatures follow distinct distributions in the limiting cases of localization and chaos. Specifically, it was shown that [20–22]

$$P_{\mathrm{POI}}(k) = \frac{\mathcal{N}_{\mathrm{POI}}}{(1+k^2)}\,, \tag{6a}$$

$$P_{\mathrm{GUE}}(k) = \frac{\mathcal{N}_{\mathrm{GUE}}}{(1+k^2)^2}\,, \tag{6b}$$

where $\mathcal{N}_{\mathrm{POI}}$ and $\mathcal{N}_{\mathrm{GUE}}$ are normalization constants and k scales the curvature κ by the average level spacing Δ and the variance of the distribution of the velocities $\partial_t\phi_n$ [21, 22] ,

$$k_n = \frac{\kappa_n \Delta(\phi_n)}{2\pi \mathrm{Var}(\partial_t\phi_n)}\,. \tag{7}$$

Both, Δ and $\mathrm{Var}(\ldots)$, are calculated for small intervals around the target phase ϕ_n. For large k, the distributions of Eq. (6) give a power-law behavior,

$$P(k\to\infty) \propto \|k\|^{-\widetilde{\beta}}\,, \tag{8}$$

with $\widetilde{\beta} = 2$ for the Poisson case and $\widetilde{\beta} = 4$ for the GUE case [11, 20, 22].

Indeed, analysis of the eigenphase curvatures corroborates the occurrence of chaotic fluctuations indicated by the statistical analysis of the eigenphase differences in Fig. 3(j)–(m): Noting the double-logarithmic scale, it is clear that small curvatures are prevalent for regular dynamics in Fig. 3(j), (k), and, to a lesser extent (m), whereas larger curvatures have significantly more weight in the region of nonlinear behavior, cf. Fig. 3(l).

To make the correspondence between the eigenphase statistics and the occurence of nonlinear/integrable dynamics more quantitative, we choose 30 equally-spaced t segments of length $0.5\,\mathrm{ns}$ and calculate the curvature of the eigenphases in each of these intervals. The resulting distributions of the curvatures are shown in Fig. 4, where the color coding corresponds to the KL divergence $D(P|P_{\mathrm{POI}})$ of the eigenphase spacing, calculated for the same time interval. The most important message that this figure conveys is that, from the perspective of curvatures, there are traces of nonlinear GUE-like dynamics for all, but the initial time intervals. Despite the fact that our spectrum exhibits only 150 levels, the curvature statistics shows general similarity to pure GUE-behavior (inset of Fig. 4) exhibiting a plateau of constant probabilities for small curvatures $k \lesssim 1$ followed by a crossover to polynomial decay of probabilities in the high curvature regime above. While our numerical data does not exhibit a perfectly flat plateau, it does

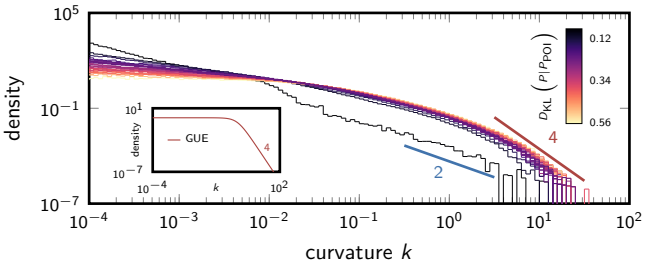

FIG. 4. **Curvature statistics** for the instantaneous eigenphases of the unitary operator U implementing the BGATE. The main panel shows a histogram of the curvature distribution where the color-coding indicates the KL divergence for the eigenphase spacing. In the high curvature regime the solid lines indicate the expected polynomial fits to the data, consistent with the GUE-like behavior (shown in the inset) of a power-law decay with exponent $\widetilde{\beta} = 4$ for all but the very first time interval which is consistent with Poisson-like behavior and an exponent of $\widetilde{\beta} = 2$.

show the more defining power-law decay for large curvatures, reproducing the GUE exponent of $\widetilde{\beta} = 4$ for all but the initial time interval. The latter instead follows a POI-like behavior with exponent $\widetilde{\beta} = 2$.

We thus find that analysis of the curvatures allows the isolation of a subset of states for which the predictions of random matrix theory apply. Remarkably, this subset of states can comprise only a small portion of Hilbert space. In such cases, the KL divergence has difficulty to indicate the onset of chaotic fluctuations, due to the low weight of the affected states in the sum over all states, cf. Eq. (4). In contrast, "sorting" the evolutions according to their curvature allows for identifying the avoided crossings that are a defining hallmark of the chaotic fluctuations.

C. Occupation dynamics

In this section, we turn from the analysis of the time-dependent spectra to the analysis of states. More precisely, we introduce and discuss several measures that are based on the population dynamics and show which of those are sensitive regarding the observed non-integrability of the dynamics.

As a first step, we consider the time occupation of the time-evolved computational basis states $|00\rangle, |01\rangle, |10\rangle, |11\rangle$. The question is whether traces of the non-integrability we observed in the time-dependent spectra are visible in the occupation of computational states. Figure 5 (a) shows that this is not the case. Tracing the occupation of a state initialized as $|00\rangle$ over the first $5\,\mathrm{ns}$ — an interval which we saw contains regions of regular and non-integrability in the window between $3\,\mathrm{ns}$ to $4\,\mathrm{ns}$ — we observe no signatures of irregularity in the occupation of states.

The occupation of single particle states close to the ground state thus does not respond to transient instabilities in the system. We may therefore rule out the plain occupation dynamics as a good indicator of non-integrability. However, one may speculate that the occupation of higher lying states may be a

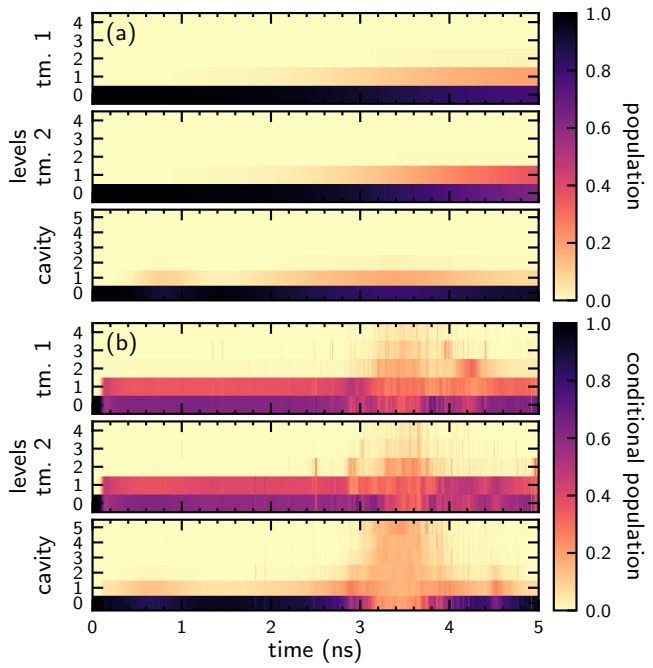

FIG. 5. **Occupation dynamics.** (a) Occupation dynamics for $|\Psi(t)\rangle = \mathsf{U}(t)\,|00\rangle$ during the first 5 ns of the BGATE. The three panels show the instantaneous, bare level occupations for $\rho_{1/2/\mathrm{c}}(t) = \mathrm{tr}_{2,\mathrm{c}/1,\mathrm{c}/1,2}\{|\Psi(t)\rangle\langle\Psi(t)|\}$ of the two transmons (with five levels per transmon) and the cavity (with six levels), respectively. (b) The conditional population dynamics, cf. Eq. (12), for the same state.

more sensitive indicator. A first question to be asked is how much of the total spectral weight carried by an evolving state actually lies outside the logical subspace. To answer it, we define

$$p_{\mathrm{sub}}(t) = \frac{1}{4}\sum_{\{|\Psi_{\mathrm{in}}\rangle\}} \left\langle \Psi_{\mathrm{in}} \right| \mathsf{U}^{\dagger}(t)\Pi_{\mathrm{sub}}\mathsf{U}(t) \left| \Psi_{\mathrm{in}} \right\rangle ,$$
$$\Pi_{\mathrm{sub}} = \sum_{\{|\Psi_{\mathrm{in}}\rangle\}} |\Psi_{\mathrm{in}}\rangle\langle\Psi_{\mathrm{in}}| ,$$

where $|\Psi_{\mathrm{in}}\rangle \in \{|00\rangle, |01\rangle, |10\rangle, |11\rangle\}$. Here, Π_{sub} is the projector onto the logical subspace and p_{sub} the time dependent probability that a state initialized as a computational state stays inside this space.

Figure 3(b) shows the population outside of the logical subspace, $1 - p_{\mathrm{sub}}(t)$, for the BGATE and the initial state $|00\rangle$. At most times this figure hovers around 10-20%, again showing no noticeable changes during the irregular time window. We conclude that the cumulative weight sitting in the non-computational state likewise is blind to dynamical instability. We thus zoom in to the next level of resolution and monitor the occupation of individual "many-body" eigenstates $\Phi_n(t)$ of the full evolution operator $\mathsf{U}(t)$. With an initial state as before, $|\Psi_{\mathrm{in}}\rangle \in \{|00\rangle, |01\rangle, |10\rangle, |11\rangle\}$, we define the probabilities

$$p_n(t) = |\langle\Phi_n(t)\,|\,\mathsf{U}(t)\,|\,\Psi_{\mathrm{in}}\rangle|^2 , \tag{9}$$

normalized as $\sum_n p_n = 1$. The color coding in Fig. 3 (c) and (d) shows the distribution of these weights over the eigenphases ϕ_n of the first 150 states of the system. In this representation, blue color is used to indicate the bare eigenphases, while a combined color coding from dark purple to light orange and dot size coding from larger to smaller dots indicates larger to smaller state occupation. This visual data indeed shows a massive fragmentation of the evolving state over a high dimensional subspace during intervals where the spectral analysis flags non-integrability (via the KL divergence). Outside these regions, the spectral weight remains concentrated on a few states in and outside the computational subspace. However, while the correlation of state fragmentation and non-integrability is a generic phenomenon, we have also observed milder forms of transient state spreading in gate protocols without chaotic instabilities, such as the slower operations shown in Fig. 2(f)–(j).

While the above data may serve as a visual indicator for dynamical signatures of non-integrability, it contains too much information to be quantitatively useful. The simplest way to condense it is to track the time dependent fraction M/N of the number of levels, M, whose occupation probability exceeds a given threshold p:

$$P_p(t) = \frac{1}{N}\sum_{n=1}^{N} \Theta(p_n(t) - p), \tag{10}$$

where Θ is the Heaviside step function. The purple line in Fig. 3(b) corresponds to $P_p(t)$ for $p = 1\%$ and thus reflects the spreading/contracting of the colored dots in Fig. 3(c). We observe that this figure, too, is relatively non-expressive in that it is qualitatively similar to the total occupation of the out-of-computational subspace $1 - P_{\mathrm{sub}}$, hinting at a limited usefulness of Eq. (10).

A more meaningful quantity is obtained by the projection of exact instantaneous eigenstates Φ_n onto select occupation eigenstates, $|i_1, i_2, i_{\mathrm{c}}\rangle_{\mathrm{Fock}}$, weighted with the occupation probabilities p_n computed according to Eq. (9),

$$P_{i_1,i_2,i_{\mathrm{c}}}(t) = \sum_n p_n(t)\,|\langle\Phi_n(t)\,|\,i_1, i_2, i_{\mathrm{c}}\rangle_{\mathrm{Fock}}|^2 , \tag{11}$$

Note that Eq. (11) is quartic in the states $\{|\Phi_n(t)\rangle\}$. (A squared amplitude is hiding in p_n.) We read these fourth moments of wave functions as a sum over conditional probabilities, where the first factor p_n states the representation of state Φ_n in the actual time evolved initial state, and the second its probability to be found in the Fock space state $|i_1, i_2, i_{\mathrm{c}}\rangle_{\mathrm{Fock}}$. These quantities can be further reduced to yield, say, the representation of the first transmon's states as

$$P_{i_1}(t) = \sum_{i_2=0}^{N_2-1}\sum_{i_{\mathrm{c}}=0}^{N_{\mathrm{c}}-1} P_{i_1,i_2,i_{\mathrm{c}}}(t) , \tag{12}$$

Fig. 5 (b) shows how this data efficiently detects the instability in the high lying sector of Hilbert space during the interval between 3 and 4 ns. In this way, it represents a good compromise between the bare occupation probabilities of the low lying states, which are blind to the presence of unstable regimes

(Fig. 5 (b)), and the excessive data carried by the full set of amplitudes $\{\Phi_n\}$.

To summarize, we have found two state population-based measures, Eqs. (9) and (12), that are sensitive to the non-integrability of the dynamics. Unfortunately, both of them require the diagonalization of $\mathsf{U}(t)$ and their computation will therefore become difficult for larger systems. In contrast, the analyses based solely upon the occupation dynamics, i.e., both level or subspace occupations, show no correlation with the observed irregularities. This suggests that such irregularities might be easily overseen if only the occupation dynamics is analyzed.

D. Robustness

Above we have characterized the time evolution of the gate in terms of various complementary pieces of information. We have used the KL divergence, the many-body state occupancy characterizing the high-lying sectors of Hilbert space, and the weighted probabilities Eq. (12) correlating this information with the occupation of low-lying states. All types of data indicate transient and recurrent regimes of instability in the time evolution. The white elephant in the room now is the question how these findings will reflect in the performance of the gate.

We first note that all gate protocols investigated here exhibit remarkably low gate errors [7], despite the complexity of their time-evolution. From the perspective of quantum optimal control, the low errors are actually not that surprising: In a finite-dimensional Hilbert space, it is sufficient to know the exact Hamiltonian that governs the system's dynamics in order to derive high-fidelity control solutions. However, the assumption of precisely knowing the Hamiltonian is not realistic. For superconducting qubits, in particular, system parameters are typically not very accurately known and moreover tend to drift over time. A realistic theoretical description must account for at least a small level of uncertainty. Similar uncertainties apply also to the control fields, due to inaccuracies in the generating hardware. We therefore now seek to quantify the robustness of the analyzed gate protocols. In particular, we would like to know whether the dynamics complexity observed above diminishes the robustness of the gate.

We therefore focus on the fast BGATE protocol where signatures of chaotic behavior have been most apparent. The working assumption is that small deviations in the Hamiltonian, or in control parameters may cause large deviations, i.e., large gate errors, in the output. In detail, we assume a constant deviation of parameters from their values for which the control field has been optimized for. We consider three scenarios: (i) a constant deviation of the transmon and cavity frequencies, in Eq. (1) reflected by deviations in $\delta_1, \delta_2, \delta_c$, (ii) a deviation in the transmon-cavity coupling strength g and (iii) a deviation in the field amplitude $\mathcal{E}(t)$.

Figure 6 shows the robustness analysis for these scenarios, quantified by the (generalized) gate error. We define the latter in terms of the local invariants functional [23] which measures how much the entangling content of the realized gate deviates from the entangling content of the BGATE. In other words,

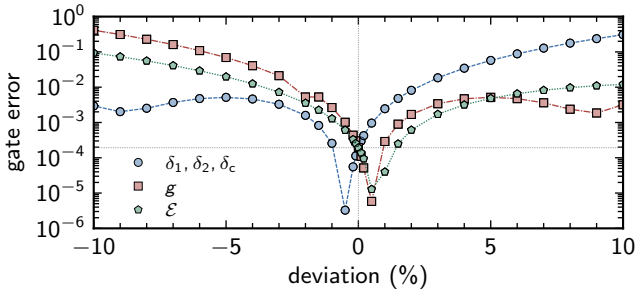

FIG. 6. **Gate error for the fast BGATE** with $T = 50\,\mathrm{ns}$ as a function of deviations in the Hamiltonian parameters. The horizontal lines indicates the gate error in the absence of any deviations.

the generalized gate error is insensitive to single-qubit rotations because these are typically easy to correct for, and its use as the figure of merit is less stringent than the standard gate error. Despite this relaxed definition of gate error, the BGATE shows high levels of sensitivity in all considered scenarios. For the detunings $\delta_1, \delta_2, \delta_c$, positive deviations on the order of 1%, which amount to actual deviations between 0.3 MHz and 3 MHz, are found to lead to an increase of one order of magnitude in the (generalized) gate error. This increases to three orders of magnitude when the deviation reaches 10%. For negative deviations, the error first drops before reaching a plateau where any deviation from -2% to -10% results in a one order of magnitude error increase. The error increase as a function of positive vs negative deviation is reversed, when considering deviations in the coupling strength g and the field amplitude $\mathcal{E}$: Negative deviations of -1% in both parameters (corresponding to changes of 0.7 MHz, resp. 1 MHz in g and $\mathcal{E}$) increase the error by one order of magnitude, shooting up to three orders of magnitude for deviations of -10%. In contrast, the gate error drops for positive deviations of up to 1% in g and $\mathcal{E}$. The drop for too large values of g ("positive deviations") is readily rationalized since a stronger coupling may be beneficial for generating the desired entangling content, which is what is measured by the generalized error. Analogously, negative deviations in g rapidly lead to an increased gate error as weaker couplings g do not allow the build-up of enough entanglement within the same time — especially for gate protocols at the quantum speed limit as analyzed here. This also explains why, out of the three parameters investigated, the sensitivity of the generalized gate error is largest for the deviations in the coupling.

The lack of robustness in the fast BGATE may be expectable for a gate showing signatures of chaotic dynamics. We note, however, that the gates of Ref. [7] have not been optimized to be robust against parameter fluctuations. Indeed, for a two-element model system where chaotic behavior has also been observed, the situation was found to be controllable [24]. It may therefore be premature to conclude that signatures of chaos in the gate dynamics categorically hamper gate robustness. At the same time, it is probably safe to say the fragmentation of spectral weight over the complex structure of the non-computational Hilbert space transiently observed during the fast protocols investigated here will not be benefi-

cial to gate robustness. It will be interesting to find out under which conditions robust fast gates can be defined nonetheless, or whether optimization may identify protocols avoiding the emergence of strong fluctuations in the spectra and states of $U(t)$. To this end, one needs to include robustness as a desired gate property when carrying out the gate optimization which is possible by means of ensemble optimization [25] at a somewhat increased numerical cost.

IV. CONCLUSIONS AND OUTLOOK

We have applied diagnostics of many-body theory – spectral statistics and statistics of many-body wavefunctions – to analyze the dynamics of transmon qubits during gate operation. Our testbed have been two universal sets of gates for transmons quasi-dispersively coupled to a cavity. The gates were designed with optimal control theory [7], with one set operating at the shortest possible duration, the so-called quantum speed limit, whereas the slower gates execute in twice that time. While a universal set only involves single-qubit and two-qubit gates, an operation at the quantum speed limit excites significant amounts of population to excited levels outside of the computational subspace. Chaotic fluctuations, if relevant, may therefore show an impact already for the comparatively small Hilbert spaces of the tripartite system.

All the gate operations that we have analyzed are carried out by applying shaped microwave pulses to the cavity that jointly couples to both qubits [7]. When applying spectral statistics to gate dynamics, one has the options to either analyze the instantaneous eigenvalues of the Hamiltonian or the eigenphases of the time-evolution operator. We have opted for the latter because it captures time non-local information. We have augmented the analysis of eigenphase differences with that of eigenphase curvatures, as another indicator of non-integrable dynamics in the time-dependent spectrum.

Both eigenphase and wavefunction statistics clearly display signatures of emergent chaos in three out of the five gates making up the fastest universal set. The remaining two gates are implemented by weaker drives and thus characterized by less population of higher excited levels. The weaker driving is also at work for the gates operating with twice the duration. These slow gates, too, barely show deviations from integrable dynamics.

Analysis of the eigenphase curvatures has turned out to be the most sensitive tool to diagnose signatures of non-integrability, due to the ability to identify the subset of states evolving through avoided crossings. More conventional measures, such as the KL divergence of the eigenphases or measures based on population dynamics, are hampered by an indiscriminate average over state space.

For those gates that are prone to chaotic fluctuations, we have made two key observations. (i) For most of the time, the dynamics is neither fully integrable nor fully chaotic. (ii) Time intervals where the statistics have a much larger match with the chaotic limit are followed by time intervals where integrable statistics are recovered. This suggests that the optimized pulses are able to steer the dynamics during a chaotic sea without compromising the gate fidelity. One should keep in mind, however, that quantum optimal control in general requires precise knowledge of the Hamiltonian and coupling to the external drive, an assumption that often is not justified, certainly not in the case of transmon qubits. Indeed, when adding fluctuations to the parameters characterizing the Hamiltonian, the gate error shoots up 1-2 orders of magnitude already for fluctuations at the level of 1-2%.

This analysis raises the question whether there is a simple connection between robustness and signatures of chaos. In other words, do robust solutions require chaotic signatures to be absent. The answer to this question is less obvious than one might conjecture at first glance. The quantum speed limit, for instance, does not impede implementation of energy-efficient quantum gates [26]. Possibly, energy-efficient quantum gates at the speed limit would be less prone to chaotic fluctuations that the gates analyzed here. To answer this question, one could, for example, repeat the gate optimization of Ref. [7] with ensemble optimization to explicitly enforce robustness [25] or to include energy efficiency as an additional time-dependent constraint [27].

ACKNOWLEDGMENTS

We thank David DiVincenzo for fruitful discussions. Financial support from the Deutsche Forschungsgemeinschaft (DFG), Project No. 277101999, CRC 183 (project C05), and the Cluster of Excellence Matter and Light for Quantum Computing (ML4Q) EXC 2004/1 – 390534769 is gratefully acknowledged.

DATA AVAILABILITY

The details of the optimized gate protocols and the numerical data shown in the figures are available on Zenodo [28].

[1] P. Krantz, M. Kjaergaard, F. Yan, T. P. Orlando, S. Gustavsson, and W. D. Oliver, A quantum engineer's guide to superconducting qubits, Applied Physics Reviews **6** (2019).

[2] J. J. García-Ripoll, *Quantum Information and Quantum Optics with Superconducting Circuits* (Cambridge University Press, 2022).

[3] C. Berke, E. Varvelis, S. Trebst, A. Altland, and D. P. DiVincenzo, Transmon platform for quantum computing challenged by chaotic fluctuations, Nat. Commun. **13**, 2495 (2022).

[4] F. W. Strauch, P. R. Johnson, A. J. Dragt, C. J. Lobb, J. R. Anderson, and F. C. Wellstood, Quantum Logic Gates for Coupled Superconducting Phase Qubits, Phys. Rev. Lett. **91**, 167005 (2003).

[5] P. Magnard, P. Kurpiers, B. Royer, T. Walter, J.-C. Besse, S. Gasparinetti, M. Pechal, J. Heinsoo, S. Storz, A. Blais, and A. Wallraff, Fast and Unconditional All-Microwave Reset of a Superconducting Qubit, Phys. Rev. Lett. **121**, 060502 (2018).

[6] S. Deffner and S. Campbell, Quantum speed limits: from Heisenberg's uncertainty principle to optimal quantum control, J. Phys. A: Math. Theor. **50**, 453001 (2017).

[7] M. H. Goerz, F. Motzoi, K. B. Whaley, and C. P. Koch, Charting the circuit QED design landscape using optimal control theory, npj Quantum Inf. **3**, 37 (2017).

[8] J. Cohen, A. Petrescu, R. Shillito, and A. Blais, Reminiscence of Classical Chaos in Driven Transmons, PRX Quantum **4**, 020312 (2023).

[9] S.-D. Börner, C. Berke, D. P. DiVincenzo, S. Trebst, and A. Altland, Classical Chaos in Quantum Computers (2023), arXiv:2304.14435.

[10] C. P. Koch, U. Boscain, T. Calarco, G. Dirr, S. Filipp, S. J. Glaser, R. Kosloff, S. Montangero, T. Schulte-Herbrüggen, D. Sugny, and F. K. Wilhelm, Quantum optimal control in quantum technologies. strategic report on current status, visions and goals for research in europe, EPJ Quantum Technol. **9**, 19 (2022), 2205.12110.

[11] S. J. Garratt, S. Roy, and J. T. Chalker, Local resonances and parametric level dynamics in the many-body localized phase, Phys. Rev. B **104**, 184203 (2021).

[12] J. Zhang, J. Vala, S. Sastry, and K. B. Whaley, Minimum Construction of Two-Qubit Quantum Operations, Phys. Rev. Lett. **93**, 020502 (2004).

[13] Note that this sorting might break continuity if a single eigenphase $\phi_n(t)$ is viewed as a function of time.

[14] V. Oganesyan and D. A. Huse, Localization of interacting fermions at high temperature, Phys. Rev. B **75**, 155111 (2007).

[15] Strictly speaking, the distribution of maximally chaotic unitary operators is governed by the circular ensembles [29]. However, where the statistics of nearby levels is concerned, this point does not matter.

[16] Y. Y. Atas, E. Bogomolny, O. Giraud, and G. Roux, Distribution of the Ratio of Consecutive Level Spacings in Random Matrix Ensembles, Phys. Rev. Lett. **110**, 084101 (2013).

[17] S. Kullback and R. A. Leibler, On Information and Sufficiency, Ann. Math. Stat. **22**, 79 (1951).

[18] B. Swingle, Unscrambling the physics of out-of-time-order correlators, Nat. Phys. **14**, 988 (2018).

[19] W. Kirkby, D. H. J. O'Dell, and J. Mumford, False signals of chaos from quantum probes, Phys. Rev. A **104**, 043308 (2021).

[20] M. Filippone, P. W. Brouwer, J. Eisert, and F. von Oppen, Drude weight fluctuations in many-body localized systems, Phys. Rev. B **94**, 201112 (2016).

[21] F. von Oppen, Exact distribution of eigenvalue curvatures of chaotic quantum systems, Phys. Rev. Lett. **73**, 798 (1994).

[22] A. Maksymov, P. Sierant, and J. Zakrzewski, Energy level dynamics across the many-body localization transition, Phys. Rev. B **99**, 224202 (2019).

[23] M. M. Müller, D. M. Reich, M. Murphy, H. Yuan, J. Vala, K. B. Whaley, T. Calarco, and C. P. Koch, Optimizing entangling quantum gates for physical systems, Phys. Rev. A **84**, 042315 (2011).

[24] A. V. Andreev, A. G. Balanov, T. M. Fromhold, M. T. Greenaway, A. E. Hramov, W. Li, V. V. Makarov, and A. M. Zagoskin, Emergence and control of complex behaviors in driven systems of interacting qubits with dissipation, npj Quantum Inf. **7**, 1 (2021).

[25] M. H. Goerz, E. J. Halperin, J. M. Aytac, C. P. Koch, and K. B. Whaley, Robustness of high-fidelity Rydberg gates with single-site addressability, Phys. Rev. A **90**, 032329 (2014).

[26] M. Aifer and S. Deffner, From quantum speed limits to energy-efficient quantum gates, New J. Phys. **24**, 055002 (2022).

[27] J. P. Palao, D. M. Reich, and C. P. Koch, Steering the optimization pathway in the control landscape using constraints, Phys. Rev. A **88**, 053409 (2013).

[28] D. Basilewitsch, S.-D. Börner, C. Berke, A. Altland, S. Trebst, and C. P. Koch, Data underpinning 'Chaotic fluctuations in a universal set of transmon qubit gates', 10.5281/zenodo.10160591 (2023).

[29] T. Guhr, A. Müller-Groeling, and H. A. Weidenmüller, Random-matrix theories in quantum physics: common concepts, Physics Reports **299**, 189 (1998).

Appendix A: Out-of-time-ordered correlators (OTOCs)

Additionally, we check so-called out-of-time-ordered correlators (OTOCs), which are a good measure for information scrambling as well as quantum chaos [18]. Let V and W be two Hermitian operators, the OTOC is given by

$$F(t) = \mathfrak{Re}\left\{\left\langle \mathsf{W}^\dagger(t)\mathsf{V}^\dagger\mathsf{W}(t)\mathsf{V}\right\rangle_\Psi\right\}, \quad \mathsf{W}(t) = \mathsf{U}^\dagger(t)\mathsf{W}\mathsf{U}(t), \tag{A1}$$

which depends on the state $|\Psi\rangle$ for which it is evaluated. If V and W are also unitary, besides being Hermitian, and fulfill $[\mathsf{V},\mathsf{W}] = 0$, we have $F(0) = 1$ for all $|\Psi\rangle$ and a deviation like $F(t) < 1$ at later times t indicates information scrambling between the two subspaces acted upon by V and W. While in two-level systems a possible choice would be $\mathsf{V},\mathsf{W} \in \{\sigma_x, \sigma_y, \sigma_z\}$ such that V and W are both Hermitian *and* unitary. Unfortunately, this is note possible in our case due to the larger Hilbert space. However, since unitarity of V and W is not a requirement, we choose

$$\mathsf{V} = \mathsf{b}_1 + \mathsf{b}_1^\dagger, \qquad \mathsf{W} = \mathsf{b}_2 + \mathsf{b}_2^\dagger \tag{A2a}$$

and

$$\mathsf{V} = \mathsf{b}_1^\dagger\mathsf{b}_1, \qquad \mathsf{W} = \mathsf{b}_2^\dagger\mathsf{b}_2. \tag{A2b}$$

Figure 7 shows the OTOCs for those two choices of W and V for all four computational basis states $|00\rangle, |01\rangle, |10\rangle, |11\rangle$ for the fast BGATE. The blue background area indicates the KL divergence with respect to the POI statistics in order to compare the course of the OTOCs to peaks in the KL divergence indicating chaotic regions. We find the OTOCs to not match the KL divergence, neither for the two choices of V and W presented in Fig. 7 nor for other choices.

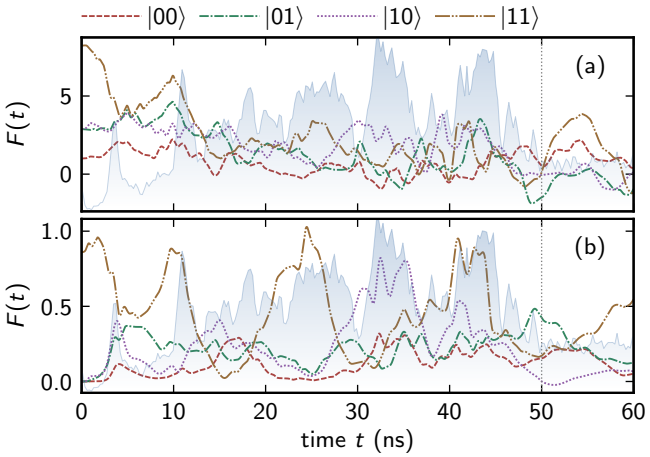

FIG. 7. **OTOCs for the fast BGATE** with $T = 50\,\mathrm{ns}$. The operators are (a) $\mathsf{V} = \mathsf{b}_1 + \mathsf{b}_1^\dagger$ and $\mathsf{W} = \mathsf{b}_2 + \mathsf{b}_2^\dagger$ as well as (b) $\mathsf{V} = \mathsf{b}_1^\dagger\mathsf{b}_1$ and $\mathsf{W} = \mathsf{b}_2^\dagger\mathsf{b}_2$. The blue area in the background indicates the KL divergence for the POI statistics from Fig. 2 (e) in arbitrary units.